Tracking the Formation and Degradation of Fatty-Acid-Accumulated Mitochondria Using Label-Free Chemical Imaging

Chi Zhang
University of Illinois at Urbana Champaign
Stephen Boppart (boppart@illinois.edu)
University of Illinois at Urbana Champaign

Research Article

Keywords: FA, organelles, mitochondrial, hypothermia

Posted Date: December 14th, 2020

DOI: https://doi.org/10.21203/rs.3.rs-119989/v1

Version of Record: A version of this preprint was published at Scientific Reports on March 23rd, 2021. See the published version at https://doi.org/10.1038/s41598-021-85795-1.

Abstract

The mitochondrion is one of the key organelles for maintaining cellular homeostasis. External environmental stimuli and internal regulatory processes alter the metabolism and functions of mitochondria. To understand these activities of mitochondria, it is critical to probe the key metabolic molecules inside these organelles. In this study, we used label-free chemical imaging modalities including coherent anti-Stokes Raman scattering and multiphoton-excited autofluorescence to study the mitochondrial activities in living cancer cells. We found that hypothermia exposure tends to induce fatty-acid (FA) accumulation in some mitochondria of MIAPaCa-2 cells. Autofluorescence images show that the FA-accumulated mitochondria also have abnormal NADH and FAD metabolism, likely induced by the dysfunction of the electron transport chain. We also found that when the cells were re-warmed to physiological temperature after a period of hypothermia, the FA-accumulated mitochondria changed their structural features, likely caused by the mitophagy process. To the best of our knowledge, this is the first time that FA accumulation in mitochondria was observed in live cells. Our research also demonstrates that multimodal label-free chemical imaging is an attractive tool to discover abnormal functions of mitochondria at the single-organelle level and can be used to quantify the dynamic changes of this organelle under perturbative conditions.

Introduction

Mitochondria are the ‘power plants’ of cells and are involved in complex metabolic activities. Proper mitochondrial function is one of the key factors in maintaining cellular metabolic homeostasis. The ability to monitor mitochondrial dynamics and function, and to visualize and quantify their chemical composition in living cells, is therefore essential. Mitochondria typically have diameters between 0.5 to 1 μm and lengths up to several microns, and can be seen under a light microscope. They can be visualized based on the refractive index difference between the organelle and the cytoplasm and their unique shape, or they can be highlighted by using fluorescent probes. However, these common ways to visualize mitochondria do not provide chemical or metabolic information. Immunofluorescence techniques can reveal the presence and amount of specific proteins associated with mitochondria, but require fixation and preprocessing of cells, and therefore cannot be used to understand extended time-lapse dynamics of these organelles. Additionally, the abovementioned imaging techniques are not selective to small metabolic molecules, such as lipids and nicotinamide adenine dinucleotide hydrogen (NADH), which are key molecules involved in mitochondrial metabolism.

Raman microscopy can distinguish mitochondria from other organelles based on their unique chemical composition and is especially selective to differentiate compositional changes of small metabolites[1–3]. However, spontaneous Raman spectroscopy has long spectral acquisition times and slow imaging speeds, making it impractical to capture highly dynamic mitochondrial activities. Coherent Raman scattering microscopy techniques, including coherent anti-Stokes Raman scattering (CARS) and stimulated Raman scattering (SRS), have significantly improved the signal level as well as the speed of Raman imaging[4–12]. Both CARS and SRS allow simultaneous chemical imaging and dynamic tracking of

cellular events[13–17]. The majority of coherent Raman microscopy studies have been focused on exploring the metabolism of lipid droplets (LDs)[14,18–24], while little has been directed toward understanding mitochondrial properties.

In this study, we used CARS microscopy to image living cancer cells and discovered heterogeneity in the chemical composition of the mitochondria. We found that some mitochondria tend to accumulate fatty acids (FAs) and show strong lipid CARS signal after hypothermia exposure, likely induced by the perturbation on FA β-oxidation. Our multimodal imaging system also revealed enrichment of NADH molecules in these 'FA-accumulated' mitochondria in the multiphoton excitation fluorescence (MPEF) channel, further demonstrating the dysfunction of these organelles. Using time-lapse CARS imaging, we followed individual mitochondria trafficking and found that these dysfunctional organelles changed structures after the cells warmed back to physiological temperature, likely caused by the mitophagy process. This research highlights label-free multimodal chemical imaging as a unique tool to visualize the changes in chemical composition and function of mitochondria at the single-organelle level. Future studies will continue to unveil the dynamic formation of stressed mitochondria under various conditions.

Results

Hyperspectral CARS imaging reveals FA-accumulated organelles in stressed cells

To image organelle dynamics in real-time, we designed an integrated multimodal CARS-MPEF microscope as depicted in Fig. 1A. A dual-output laser system was used as the light source for both CARS and MPEF. The fixed-wavelength 1040 nm output was used as the Stokes beam while the wavelength-tunable output was used as the pump beam for CARS. To image lipids in the cells, we tuned the pump beam to 800 nm, corresponding to the Raman shift centered at 2884 cm^{-1}. For CARS imaging, we first spatially and temporally combined the pump and Stokes beams before chirping the beams using two SF-10 glass rods (each 150 mm long). The combined and chirped beams were guided to a 2D galvo scanning system. A 40X water immersion objective lens (Olympus, LUMPlanFl, NA = 0.8) was used to focus the laser beams onto live cells cultured on glass-bottom dishes. A dish heater was installed to control the temperature at the sample. CARS signals were acquired in the forward direction using a photo-multiplier tube (PMT, Hamamatsu S3994), while MPEF signals were collected in the epi direction using separate PMTs. For MPEF imaging of autofluorescent molecules, femtosecond laser pulses were directly used for two-photon excitation and no glass rods were implemented. Hyperspectral CARS spectra were derived using a spectral-focusing method by tuning the optical delay between the two chirped beams while collecting a single-color CARS image at each delay step[25–27].

To better visualize mitochondrial structure and dynamics, we implemented a denoising method (CANDLE-J, ImageJ-based denoising plugin) to improve the quality of the CARS images[28]. To perform denoising, a

stack of 100 time-lapse images was used (see Fig. 1B). The denoised images give better contrast for selecting the best regions of interest for hyperspectral CARS analysis.

MIAPaCa-2 cells were removed from an incubator and exposured to room temperature (24 °C) for about 1 hr prior to imaging the cells with the CARS microscope. We discovered the formation of rod-like structures in the cells, having strong signals in the lipid CH_2 vibration (see Fig. 1C, inside the yellow square). A denoised image from the same region gives better contrast to highlight the lipid-accumulated rod-like structures (Fig. 1D). Figures 1E and 1F are magnified original and denoised images from the yellow squares in Figs. 1C and 1D, respectively, in which the bright rod-like organelles are visible (see arrows). The time-lapse images of this region shown in Fig. 1G reveal that these rod-like structures were transported as whole units over time, which differentiates them from aggregates of LDs, which appear as round 'dots' in cells and usually undergo rapid contact and dissociation over time. We first fixed the cells and acquired hyperspectral CARS images, after which we compared the CARS spectra in the C-H region for different organelles in the cells. We found that a lipid-rich rod-like organelle (see ROI 1) presents a weaker CH_2 stretching CARS signal at 2850 cm^{-1} than the LDs, but a stronger CH_2 signal than the structure having very similar shape and size (see ROI 2) next to it (see Fig. 1H-J). However, if we compare the CH_3 CARS signal at 2940 cm^{-1}, the two rod-like structures have very similar intensities (Fig. 1J). Since lipids have long acyl chains with abundant CH_2 moieties, while proteins have much less CH_2 groups but a much higher portion of CH_3 groups, our observation indicates the bright rod-like structures accumulated much more lipid molecules compared to other darker rod-like organelles, but still had less lipid composition than the LDs.

Mitochondrion-specific fluorescent-labeling verifies mitochondria structures

To verify the structures of these organelles, we used standard fluorescence labeling. We added a mitochondria-targeted dye solution (MitoTracker® Green, Cell Signaling) into the culture medium of living MIAPaCa-2 cells and maintained them for 1 hr at room temperature (24 °C) before imaging. As shown in Fig. 2A-C, a rod-like organelle having stronger CH_2 signals in the CARS channel also showed a strong fluorescence signal from the MitoTracker® Green in the MPEF channel 1 (571±72 nm). This is distinctly different from the LDs, which are dot-like organelles that exhibit a very strong signal in the CARS channel but no signal in the MPEF channel. Figure 2D shows magnified images from the highlighted square areas in the CARS and the CARS/MPEF channels.

We also used immunofluorescence to further confirm the mitochondria structures. We applied the anti-adenosine triphosphate synthase subunit beta (ATPB) antibody to target the ATP synthase in mitochondria. We then applied an Alex Fluor 488 secondary antibody (ab150113, Abcam) to visualize the mitochondria in our MPEF channel 1 (571 ± 72 nm). We compared CARS and MPEF images and selected three locations to compare the CARS spectra. The spectral signatures of LDs, mitochondria with high CH_2 signals, and mitochondria with low CH_2 signals (see Fig. 2H) show similar relationships as compared to

our previously shown results (see Fig. 1J). Here, the CH_2 signal differences from the mitochondria are reduced, likely due to the use of detergents which may have washed away some lipid molecules during the sample preparation.

Therefore, we hypothesize that the rod-like structures with strong CH_2 signals are mitochondria. Mitochondria are typically protein-rich and generate weaker signals in the CH_2 vibrations. The stronger CH_2 CARS signals generated by some of these mitochondria indicate the accumulation of FA molecules in these organelles, which is observed for the first time. For MIAPaCa-2 cells, these structures were not observed in the physiological temperature (37 °C) but only detected after the 24 °C hypothermia exposure.

Multiphoton autofluorescence reveals altered NADH metabolism

Mitochondria are key regulators of cellular NADH molecules. We wanted to explore if the fatty-acid-accumulated mitochondria also have abnormal NADH metabolism. NADH molecules are autofluorescent and can be excited by the 800 nm pulses through two-photon absorption and by 1040 nm pulses through three-photon absorption[29,30]. To ensure sufficient excitation efficiency for the NADH autofluorescence, we used femtosecond laser pulses directly for both MPEF and CARS. We removed the glass rods used for hyperspectral CARS imaging in previous experiments and directly used the laser output at 800 nm and 1040 nm for CARS and MPEF. We found that the lipid-accumulated mitochondria structures show strong signals in both the transmission CARS channel and the epi-direction MPEF channel 2 (451±103 nm) which detects the NADH autofluorescence emission band (Figs. 3A-C). Figures 3D-F show magnified areas in Figs. 3A-C, highlighting a target of interest (yellow arrow).

Figure 3G compares the CARS and NADH MPEF signal intensities of LDs, FA-accumulated mitochondria, and normal mitochondria. We found that FA-accumulated mitochondria have much higher lipid and NADH signals compared to normal mitochondria. Figure 3H plots the lipid (CARS) and NADH (MPEF) signals from the three types of organelles in a 2D space for better visualization and comparison. The lipid and NADH signal intensity differences allow one to distinguish these different types of organelles, especially the FA-accumulated mitochondria, which have very different optical signatures compared to the LDs and normal mitochondria. Figure 3I compares the intensity ratio of NADH MPEF signals and the CARS signals of the three organelles (the ratio has an arbitrary unit), from which we can further distinguish the FA-accumulated mitochondria from other organelles.

Figure 3J depicts FA and NADH metabolic pathways of mitochondria. It is reasonable to believe that hypothermia impacted the electron transport chain, which converts NADH to NAD^+, and subsequently induces the accumulation of NADH in the organelles. The increased concentration of NADH possibly slows down the FA β-oxidation since NADH is the net product of this catabolic process, thus resulting in the accumulation of FA in the mitochondria.

We also compared the flavin adenine dinucleotide (FAD) level of the FA-accumulated mitochondria using the MPEF channel 1 (571±72 nm), and also found the accumulation of FAD molecules in these organelles (Figs. S1B and S1E). If we take the intensity ratio of NADH/(NADH + FAD), which is defined as the redox ratio, we find that these FA-accumulated mitochondria tend to have a higher value than other parts of the cell (Figs. S1C and S1F), indicating an abnormal redox metabolism of these organelles.

Degradation of FA-accumulated mitochondria at 37 °C

We found that hypothermia can induce the accumulation of FA and NADH in certain mitochondria of MIAPaCa-2 cells. These changes in organelle metabolism resulted in organelle dysfunction which might be toxic to cells. One of our recent studies showed that the LD dynamics of MIAPaCa-2 cells tend to recover quickly after a short term hypothermia exposure[31], suggesting that the cells develop mechanisms to recover from metabolic changes induced by hypothermia exposure. Therefore, it is reasonable to believe that cells can remove and degrade these dysfunctional mitochondria after being heated back to 37 °C.

To observe the degradation process, we first created a hypothermia condition, allowing FA-accumulated mitochondria to form, as shown in Fig. 4A. In a MIAPaCa2 cell, we first identified 3 FA-accumulated mitochondria (see red, blue, and yellow arrows) and set this time as time 0. We found that these mitochondria underwent fission and fusion (156.2 s -200.2 s), which is a common behavior when mitochondria are under stress conditions[32–34]. Later, at 220 s, the fourth FA-accumulated mitochondrion (see green arrows) appeared. At time 340 s, we reheated the sample back to 37 °C. Starting from about 619.4 s, slightly less than 300 s after the reheating started, the rod-like organelles started to form into dot-like structures (Fig. 4B-C, the blue arrow first, the red arrow second, the yellow arrow next, and the green arrow last). Eventually, all the 4 identified FA-rich mitochondria were converted to bright dot-like structures in the CARS images (Fig. 4D). This process is likely the mitophagy process during which mitochondria are wrapped by autophagosomes and eventually degraded by the cells[35–37]. Videos of FA-rich mitochondria changes can be found in the Supplementary Information. These stress-induced organelles are rich in lipid and are likely recycled by the cell.

Discussion

We believe this is the first time that FA-accumulation in mitochondria has been observed, and dynamically tracked over time in living cells. Such an abnormal metabolic signature is likely caused by the dysfunction of the electron transport chain, which is the primary process converting NAD^+ to NADH. This phenomenon was only observed following hypothermia exposure, indicating that lower temperatures tend to perturb the proper function of oxidative phosphorylation. It was reported that ADP phosphorylation is much more efficient at physiological temperature[38]. Studies also found that at lower temperatures, the maximum respiratory rates for the membrane-bound complexes were significantly reduced compared to those at the physiological temperature[39]. The increased concentration of NADH and FAD might slow down the β-oxidation process, causing the accumulation of FAs in these

mitochondria[40,41]. Hypothermia might also directly affect the β-oxidation process by reducing the activity of the related enzymes[42]. Future research focusing on the inhibition and genetic knockdown of β-oxidation-related enzymes would further clarify the causes of FA-accumulation in mitochondria under hypothermia conditions.

To form FA-accumulated mitochondria, we exposed the MIAPaCa-2 cells to room temperature for 30–60 min. Based on our empirical observations, FA accumulation in dysfunctional mitochondria tends to form within an hour. Regarding the degradation, we found the change of FA-rich mitochondria started approximately 250–500 s after rewarming began. If taking the temperature rise time into account, we believe that the autophagy process starts self-degradation faster than this time period. Our label-free chemical imaging platform offers a way to estimate the triggering time of a single autophagosome in live cells without labeling.

The FA-accumulation does not happen in all, but in only a few mitochondrial structures in MIAPaCa-2 cells during hypothermia exposure. This limited perturbation effect likely assures the survival of cells in the hypothermia condition, and the recovery of cells after rewarming back to physiological temperature. Our results also indicate that not all the LD-like structures in the cells after environmental stress are LDs. Some of the bright dot-like structures in CARS images showing up in the CH_2 vibrational channel (Fig. 4D) might originate from the dysfunctional mitochondria. These structures are likely to have different spontaneous Raman and CARS spectra compared to LDs. In the future, we will design experiments to identify and separate these mitophagosome structures using spectroscopic Raman techniques.

While we have observed FA accumulation in mitochondria, we have limited information to understand what specific types of FA are accumulated. Spontaneous Raman spectroscopy, which provides more spectral information compared to CARS, might give more spectroscopic data to probe the lipid types related to this process. To pinpoint a specific mitochondrion and collect its spontaneous Raman spectrum, we need a multimodal system with both spontaneous Raman and coherent Raman modalities, where the coherent Raman can be used to find the organelle of interest, and the spontaneous Raman can be used to provide a broader-range high-resolution Raman spectrum. Such an integrated system has been reported by other groups and will be designed and built for our future studies[43].

Methods

Coherent anti-Stokes Raman scattering and multiphoton excitation fluorescence microscopy

Our multimodal nonlinear optical microscope integrating CARS and MPEF imaging modalities was built based on a commercial microscope frame (BX51, Olympus). A dual-output femtosecond laser system (Chameleon Discovery, Coherent Inc.) was used as the light source for signal excitation. The 1040 nm fixed wavelength output was used as the Stokes beam for CARS, while the other wavelength-tunable beam was tuned to 800 nm and used as the pump beam for CARS to excite the Raman transition at

2884 cm^{-1}. MPEF excitation of NADH was primarily from two-photon absorption of the 800 nm beam, while the MPEF excitation of FAD was contributed by the nondegenerate two-photon process from the simultaneous absorption of both the 800 nm and the 1040 nm beams. The two beams were combined spatially by a dichroic beam splitter (Di02-980, Semrock) and temporally by a motorized translational stage (X-LSM050A-KX13A, Zabor Technologies Inc.). We chirped the combined pump and Stokes beams to ~ 1 ps and ~ 2 ps, respectively, by letting the combined beams pass through two SF-10 glass rods (each 150 mm long, Lattice Electro-Optics). To perform hyperspectral imaging, the motorized delay stage was swept through a 1 mm range with 10 μm per step while a single-color CARS image was acquired at each step.

A 2D galvo scanning system (8351K, Cambridge technology) was used to raster scan the laser beams at the sample. The water immersion objective lens used in the experiment (LUMPLFLN 40X, NA = 0.8, Olympus) was directly dipped into the culture media in cell culture dishes (μ-Dish 35 mm, Ibidi). A stage-top dish heater (DH-35iL, culture dish incubator, Warner Instruments) was installed to control the temperature at the sample. To maintain the temperature and avoid media evaporation, wet tissue paper was used to cover the open areas of the dish when the heating began. Three PMTs (H7422P, Hamamatsu) were used to acquire CARS and MPEF signals. CARS signals were acquired in the forward direction, while MPEF signals were collected in the epi direction. The two MPEF channels including channel 1 (571±72 nm) and channel 2 (451±103 nm) were installed to simultaneously collect MPEF signals at different wavelength ranges. A black curtain was used to cover the microscope and the detectors to reduce ambient light from leaking into the PMTs. The room lights were turned off during imaging. CARS or MPEF signals detected by the PMTs were pre-amplified by a current-voltage converter and pre-amplifier (PMT-4V3, Advanced Research Instruments Corp.). Then, the amplified signals were acquired by the data acquisition system (BNC-2110 and PCIe-6351, National Instruments). The laser scanning and image acquisition were controlled by lab-written software based on LabVIEW.

Image data analysis

Single-frame or time-lapse images were acquired at a speed of 10 μs per pixel, and each image frame contained 400 by 400 pixels. Typically, the acquisition time for each CARS or MPEF image was 2.2 s. The images were saved in the .txt format. Each time-lapse sequence contained 100 2D frames. Image processing such as pseudo color conversion, channel merging, intensity value measurement, and video conversion was performed by ImageJ functions. CARS spectra data from different locations were measured by ImageJ and plotted using Origin 2020. Image size calibration was performed using 1 μm polystyrene fluorescent beads and a resolution target.

CANDLE-J denoising

CANDLE-J denoising was performed by ImageJ. The original image stack (100 frames) was first saved in .tiff format and then imported to ImageJ by selecting the CANDLE-J plugin. The smoothing parameters, patch radius, and search volume radius used in the processing were 0.1, 2.0, and 3.0, respectively. Denoised images were saved as .png or .avi for display.

Fluorescent labeling

MitoTracker® Green was purchased from Cell Signaling Technology and used according to manufacturer instructions. A stock solution of the MitoTracker at 1 mM was directly added to the culture media to reach a final concentration of 400 nM, and incubated for 30 min before imaging.

Anti-ATPB antibody [3D5] (ab14730, mouse monoclonal, Abcam) was used to label the mitochondria ATP synthase. Goat anti-mouse IgG Alexa Fluor® 488 (ab150113, Abcam) was used as the secondary antibody to visualize the ATP synthase. The cells were first fixed for 30 min using formalin and then rinsed with phosphate-buffered saline (PBS) 3 times for 5 min each. Next, a blocking buffer (1X PBS/5% normal serum/0.3% Triton™ X-100) was used to treat the cells for 60 min. After blocking, the primary antibody was applied with a final concentration of 2 μg/mL. The samples were then stored overnight at 4 °C. Next, the sample was rinsed 3 times with 1X PBS for 5 min each. The secondary antibody stock solution with a concentration of 2 mg/mL was directly applied to the sample with a 1/500 dilution for 1 h to stain the ATP synthase. The sample was then rinsed before imaging.

Declarations

Acknowledgments

The authors thank Aneesh Alex, Jang Hyuk Lee, and Jose Rico-Jimenez from the Center for Optical Molecular Imaging for the initial installation of the laser and data acquisition/PC systems, and thank GlaxoSmithKline for the sponsored research support of the Center. We also thank Darold Spillman for lab management and information technology support. This research was financially supported in part by grants from the NIH (R01CA241618, R01EB023232) and the NSF (CBET 18-41539). Additional information can be found at http://biophotonics.illinois.edu.

Author contributions

C.Z. and S.A.B. designed research. C.Z. carried out experiments and data analysis. C.Z. and S.A.B wrote the paper. S.A.B. obtained funding for the research.

Additional information

[#]Present address:

Department of Chemistry, Purdue University, 560 Oval Drive, West Lafayette, IN 47907.

Competing interests

Stephen Boppart is a co-founder and consultant of LiveBx, Champaign, IL, which is licensing intellectual property from the University of Illinois at Urbana-Champaign to develop novel optical sources and label-

free multimodal multiphoton imaging platforms for biological and medical applications. Chi Zhang declares no competing interests.

References

1. Chiu, L.-d., Ando, M. & Hamaguchi, H.-o. Study of the 'Raman spectroscopic signature of life'in mitochondria isolated from budding yeast. *J. Raman Spectrosc.* **41**, 2–3 (2010).
2. Okada, M. *et al.* Label-free Raman observation of cytochrome c dynamics during apoptosis. *Proc. Natl. Acad. Sci. U. S. A.* **109**, 28–32 (2012).
3. Brazhe, N. A., Treiman, M., Brazhe, A. R., Maksimov, G. V. & Sosnovtseva, O. V. Mapping of redox state of mitochondrial cytochromes in live cardiomyocytes using Raman microspectroscopy. *PLoS One* **7**, e41990 (2012).
4. Cheng, J.-X. & Xie, X. S. Coherent anti-Stokes Raman scattering microscopy: instrumentation, theory, and applications. *J. Phys. Chem. B* **108**, 827–840 (2004).
5. Evans, C. L. & Xie, X. S. Coherent anti-Stokes Raman scattering microscopy: chemical imaging for biology and medicine. *Annu. Rev. Anal. Chem.* **1**, 883–909 (2008).
6. Freudiger, C. W. *et al.* Label-free biomedical imaging with high sensitivity by stimulated Raman scattering microscopy. *Science* **322**, 1857–1861 (2008).
7. Zhang, D., Wang, P., Slipchenko, M. N. & Cheng, J.-X. Fast vibrational imaging of single cells and tissues by stimulated Raman scattering microscopy. *Acc. Chem. Res.* **47**, 2282–2290 (2014).
8. Fu, D. *et al.* Quantitative chemical imaging with multiplex stimulated Raman scattering microscopy. *J. Am. Chem. Soc.* **134**, 3623–3626 (2012).
9. Potma, E. O., Evans, C. L. & Xie, X. S. Heterodyne coherent anti-Stokes Raman scattering (CARS) imaging. *Opt. Lett.* **31**, 241–243 (2006).
10. Chowdary, P. D. *et al.* High speed nonlinear interferometric vibrational analysis of lipids by spectral decomposition. *Anal. Chem.* **82**, 3812–3818 (2010).
11. Marks, D. L. & Boppart, S. A. Nonlinear interferometric vibrational imaging. *Physical Review Letters* **92**, 123905 (2004).
12. Jones, G. W., Marks, D. L., Vinegoni, C. & Boppart, S. A. High-spectral-resolution coherent anti-Stokes Raman scattering with interferometrically detected broadband chirped pulses. *Opt. Lett.* **31**, 1543–1545 (2006).
13. Shi, L. *et al.* Optical imaging of metabolic dynamics in animals. *Nat. Commun.* **9**, 1–17 (2018).
14. Nan, X., Cheng, J.-X. & Xie, X. S. Vibrational imaging of lipid droplets in live fibroblast cells with coherent anti-Stokes Raman scattering microscopy. *J. Lipid Res.* **44**, 2202–2208 (2003).
15. Zhang, C., Li, J., Lan, L. & Cheng, J.-X. Quantification of lipid metabolism in living cells through the dynamics of lipid droplets measured by stimulated Raman scattering imaging. *Anal. Chem.* **89**, 4502–4507 (2017).

16. Dou, W., Zhang, D., Jung, Y., Cheng, J.-X. & Umulis, D. M. Label-free imaging of lipid-droplet intracellular motion in early Drosophila embryos using femtosecond-stimulated Raman loss microscopy. *Biophys. J.* **102**, 1666–1675 (2012).
17. Marks, D. L., Vinegoni, C., Bredfeldt, J. S. & Boppart, S. A. Interferometric differentiation between resonant coherent anti-Stokes Raman scattering and nonresonant four-wave-mixing processes. *Appl. Phys. Lett.* **85**, 5787–5789 (2004).
18. Hellerer, T. *et al.* Monitoring of lipid storage in *Caenorhabditis elegans* using coherent anti-Stokes Raman scattering (CARS) microscopy. *Proc. Natl. Acad. Sci. U. S. A.* **104**, 14658–14663 (2007).
19. Di Napoli, C. *et al.* Quantitative spatiotemporal chemical profiling of individual lipid droplets by hyperspectral CARS microscopy in living human adipose-derived stem cells. *Anal. Chem.* **88**, 3677–3685 (2016).
20. Wang, P. *et al.* Imaging lipid metabolism in live *Caenorhabditis elegans* using fingerprint vibrations. *Angew. Chem. Int. Ed* **126**, 11981–11986 (2014).
21. Yu, Y., Ramachandran, P. V. & Wang, M. C. Shedding new light on lipid functions with CARS and SRS microscopy. *Biochim. Biophys. Acta* **1841**, 1120–1129 (2014).
22. Yue, S. *et al.* Cholesteryl ester accumulation induced by PTEN loss and PI3K/AKT activation underlies human prostate cancer aggressiveness. *Cell Metab.* **19**, 393–406 (2014).
23. Li, J. *et al.* Lipid desaturation is a metabolic marker and therapeutic target of ovarian cancer stem cells. *Cell Stem Cell* **20**, 303–314. e305 (2017).
24. Benalcazar, W. A. & Boppart, S. A. Nonlinear interferometric vibrational imaging for fast label-free visualization of molecular domains in skin. *Anal. Bioanal. Chem.* **400**, 2817–2825 (2011).
25. Rocha-Mendoza, I., Langbein, W. & Borri, P. Coherent anti-Stokes Raman microspectroscopy using spectral focusing with glass dispersion. *Appl. Phys. Lett.* **93**, 201103 (2008).
26. Langbein, W., Rocha-Mendoza, I. & Borri, P. Coherent anti-Stokes Raman micro-spectroscopy using spectral focusing: theory and experiment. *J. Raman Spectrosc.* **40**, 800–808 (2009).
27. Fu, D., Holtom, G., Freudiger, C., Zhang, X. & Xie, X. S. Hyperspectral imaging with stimulated Raman scattering by chirped femtosecond lasers. *J. Phys. Chem. B* **117**, 4634–4640 (2013).
28. Coupé, P., Munz, M., Manjón, J. V., Ruthazer, E. S. & Collins, D. L. A CANDLE for a deeper in vivo insight. *Med. Image Anal.* **16**, 849–864 (2012).
29. Tu, H. *et al.* Stain-free histopathology by programmable supercontinuum pulses. *Nat. Photonics* **10**, 534–540 (2016).
30. You, S. *et al.* Intravital imaging by simultaneous label-free autofluorescence-multiharmonic microscopy. *Nat. Commun.* **9**, 1–9 (2018).
31. Zhang, C. & Boppart, S. A. Dynamic signatures of lipid droplets as new markers to quantify cellular metabolic changes. *Anal. Chem*, in press, https://doi.org/10.1021/acs.analchem.0c03366 (2020).
32. Youle, R. J. & Van Der Bliek, A. M. Mitochondrial fission, fusion, and stress. *Science* **337**, 1062–1065 (2012).

33. Eisner, V., Picard, M. & Hajnóczky, G. Mitochondrial dynamics in adaptive and maladaptive cellular stress responses. *Nat. Cell Biol.* **20**, 755–765 (2018).
34. Kubli, D. A. & Gustafsson, Å. B. Mitochondria and mitophagy: the yin and yang of cell death control. *Circ. Res.* **111**, 1208–1221 (2012).
35. Youle, R. J. & Narendra, D. P. Mechanisms of mitophagy. *Nat. Rev. Mol. Cell Biol.* **12**, 9–14 (2011).
36. Kim, I., Rodriguez-Enriquez, S. & Lemasters, J. J. Selective degradation of mitochondria by mitophagy. *Arch. Biochem. Biophys* **462**, 245–253 (2007).
37. Pickles, S., Vigié, P. & Youle, R. J. Mitophagy and quality control mechanisms in mitochondrial maintenance. *Curr. Biol.* **28**, R170-R185 (2018).
38. Lee, M. P. & Gear, A. R. The effect of temperature on mitochondrial membrane-linked reactions. *J. Biol. Chem.* **249**, 7541–7549 (1974).
39. Pamenter, M. E., Lau, G. Y. & Richards, J. G. Effects of cold on murine brain mitochondrial function. *PLoS One* **13**, e0208453 (2018).
40. Watmough, N. *et al.* Impaired mitochondrial beta-oxidation in a patient with an abnormality of the respiratory chain. Studies in skeletal muscle mitochondria. *J. Clin. Invest.* **85**, 177–184 (1990).
41. Wang, Y. *et al.* Mitochondrial fatty acid oxidation and the electron transport chain comprise a multifunctional mitochondrial protein complex. *J. Biol. Chem.* **294**, 12380–12391 (2019).
42. Zoladz, J. A. *et al.* Effect of temperature on fatty acid metabolism in skeletal muscle mitochondria of untrained and endurance-trained rats. *PLoS One* **12**, e0189456 (2017).
43. Slipchenko, M. N., Le, T. T., Chen, H. & Cheng, J.-X. High-speed vibrational imaging and spectral analysis of lipid bodies by compound Raman microscopy. *J. Phys. Chem. B* **113**, 7681–7686 (2009).

Figures

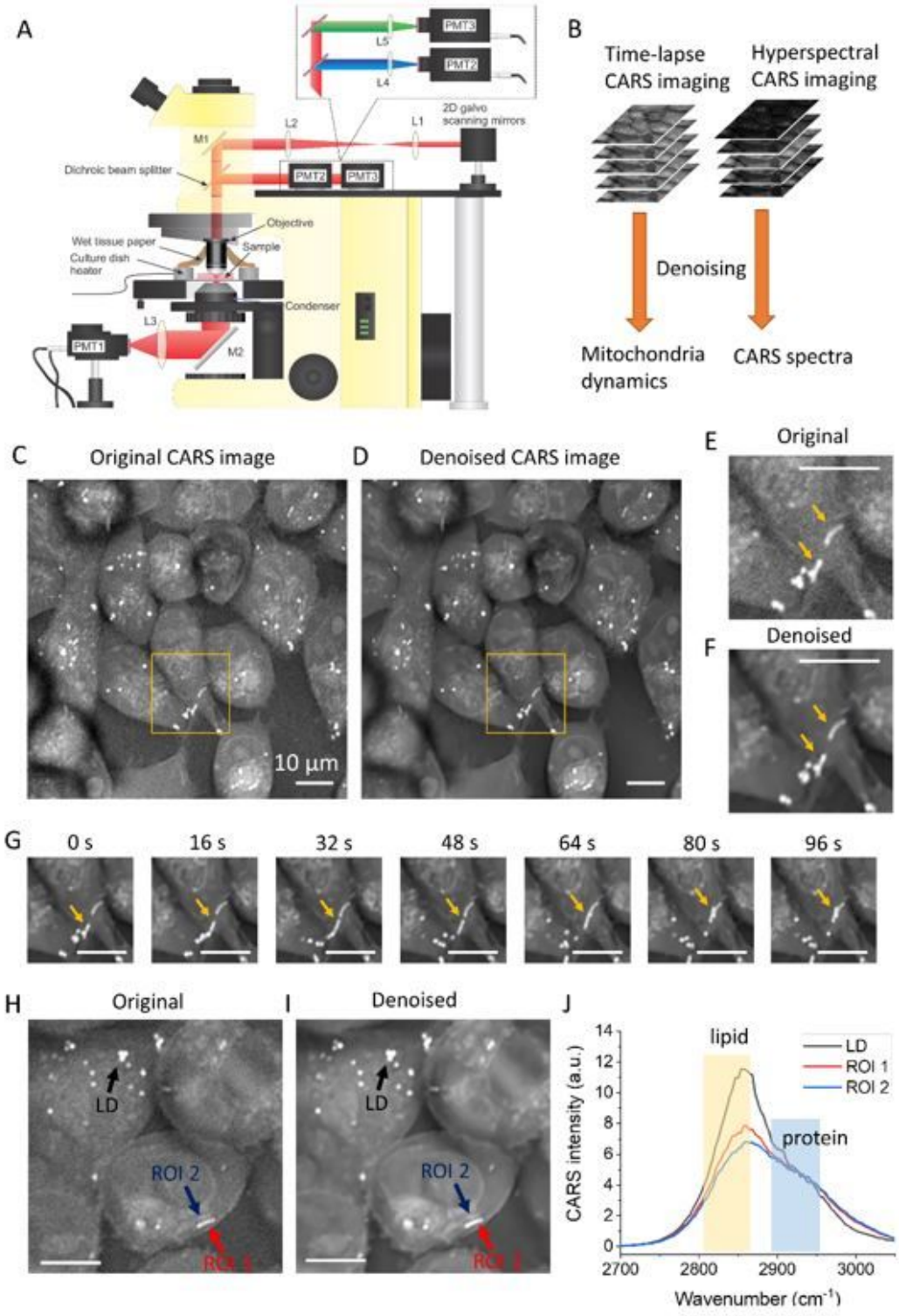

Figure 1

Discovery of fatty-acid-accumulated mitochondria in living cancer cells during hypothermia exposure. (A) Schematic of our CARS/MPEF hybrid microscope. (B) Illustration of denoising for hyperspectral and time-lapse image stacks. (C) An original CARS image at CH2 vibration frequency from MIAPaCa-2 cells after hypothermia exposure. (D) Denoised CARS image in panel (C). (E,F) Magnified areas indicated by the yellow boxes in panels (C,D), respectively. (G) Time-lapse image of the selected area in panel (D). Yellow

arrows in panels (E-G) point to FA-accumulated mitochondria structures. (H) and (I) are the original and the denoised images of fixed MIAPaCa-2 cells after hypothermia exposure. Different arrows point to different targets and regions of interest (ROIs) in these images. (J) The original CARS spectra obtained from the hyperspectral imaging. The yellow and blue bars highlight the lipid CH2 and protein CH3 vibrational regions. PMT, photomultiplier tube; M, mirror; L, lens. Scale bars represent 10 μm and apply to all images.

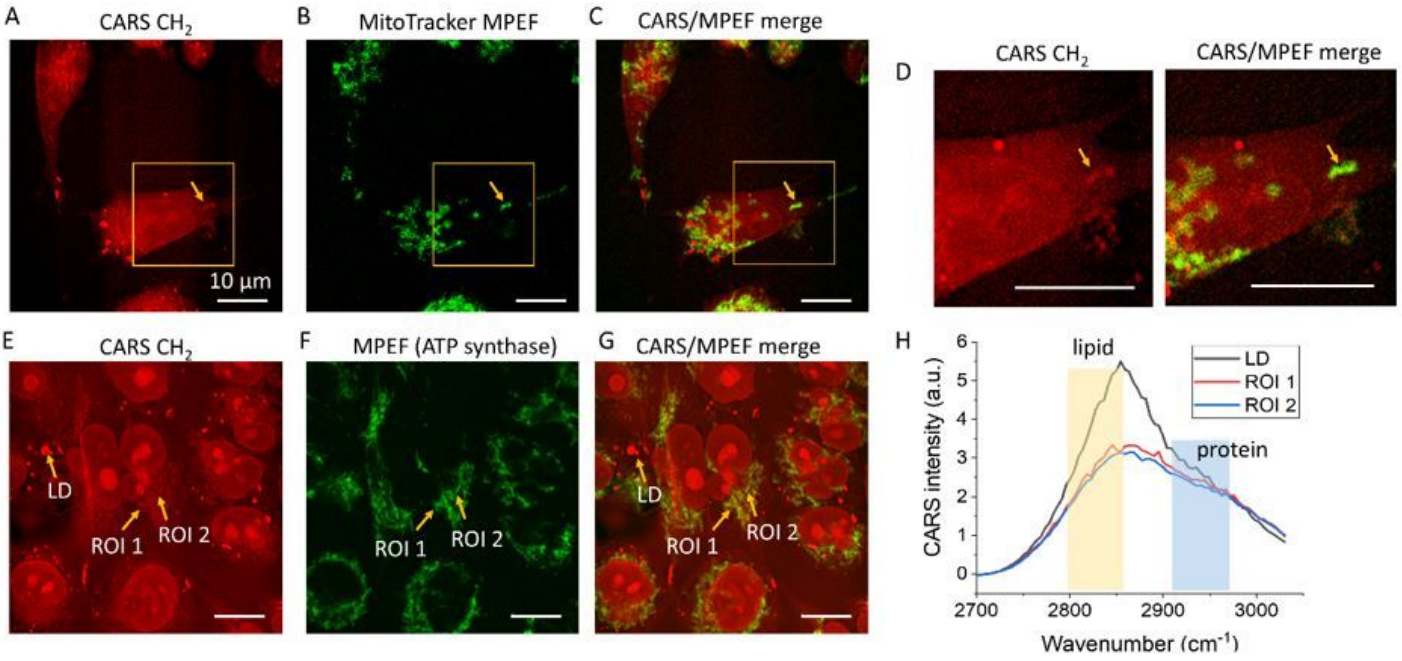

Figure 2

Verifying mitochondrial structures using fluorescent labeling. (A-C) CARS, MPEF, and CARS/MPEF composite images of MitoTracker® labeled live MIAPaCa-2 cells. Arrows point out the target of interest. (D) Magnified images of areas indicated by the yellow boxes in panels (A) and (C). (E-G) CARS, MPEF, and CARS/MPEF composite images of immunofluorescence labeled (anti-ATPB) MIAPaCa-2 cells, respectively. Different arrows point to different targets and regions of interest (ROIs) in these images. (H) The original CARS spectra obtained from hyperspectral imaging. Scale bars represent 10 μm and apply to all images.

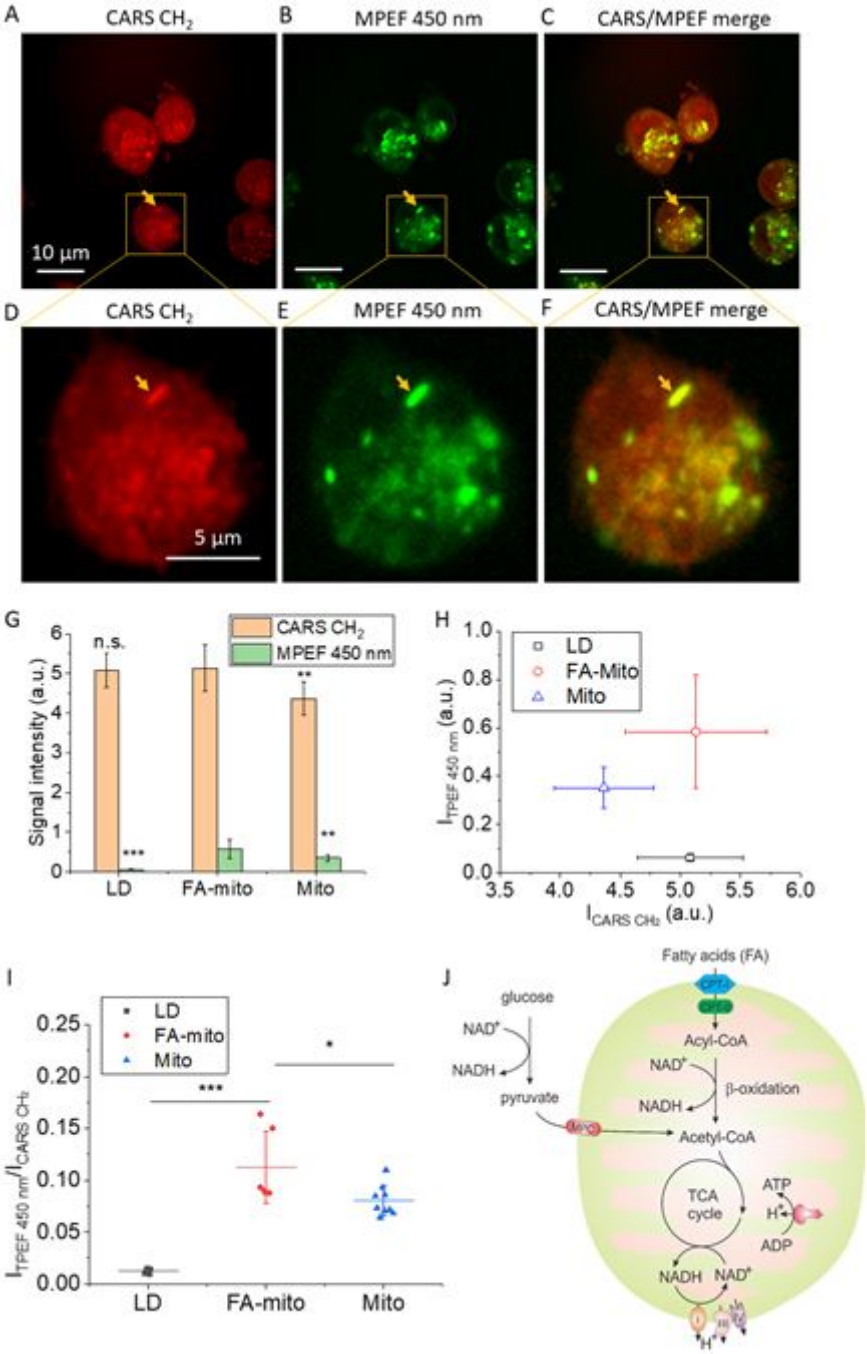

Figure 3

MPEF imaging revealed abnormal NADH signals in the fatty-acid-accumulated mitochondira. (A-C) CARS, MPEF, and CARS/MPEF composite images of MIAPaCa-2 cells. The MPEF detects MPEF signals from NADH centered at 450 nm. (D-F) Magnified selected areas in panels (A-C), respectively. Yellow arrows point to targets of interest. (G) CARS and MPEF signal intensities (arbitrary units) of LD, FA-accumulated mitochondria, and normal mitochondria in MIAPaCa-2 cells. (H) 2D plots of the CARS and MPEF intensities of the three organelles analyzed in panel (G). (I) Intensity ratios of MPEF/CARS of the three organelles. (J) Illustration of NADH metabolism related to the mitochondrion. For the Student's t-test in (G), n=5; and in (I), n=6. n.s., $p>0.05$; *, $p\leq0.05$; **, $p\leq0.01$; ***, $p\leq0.001$.

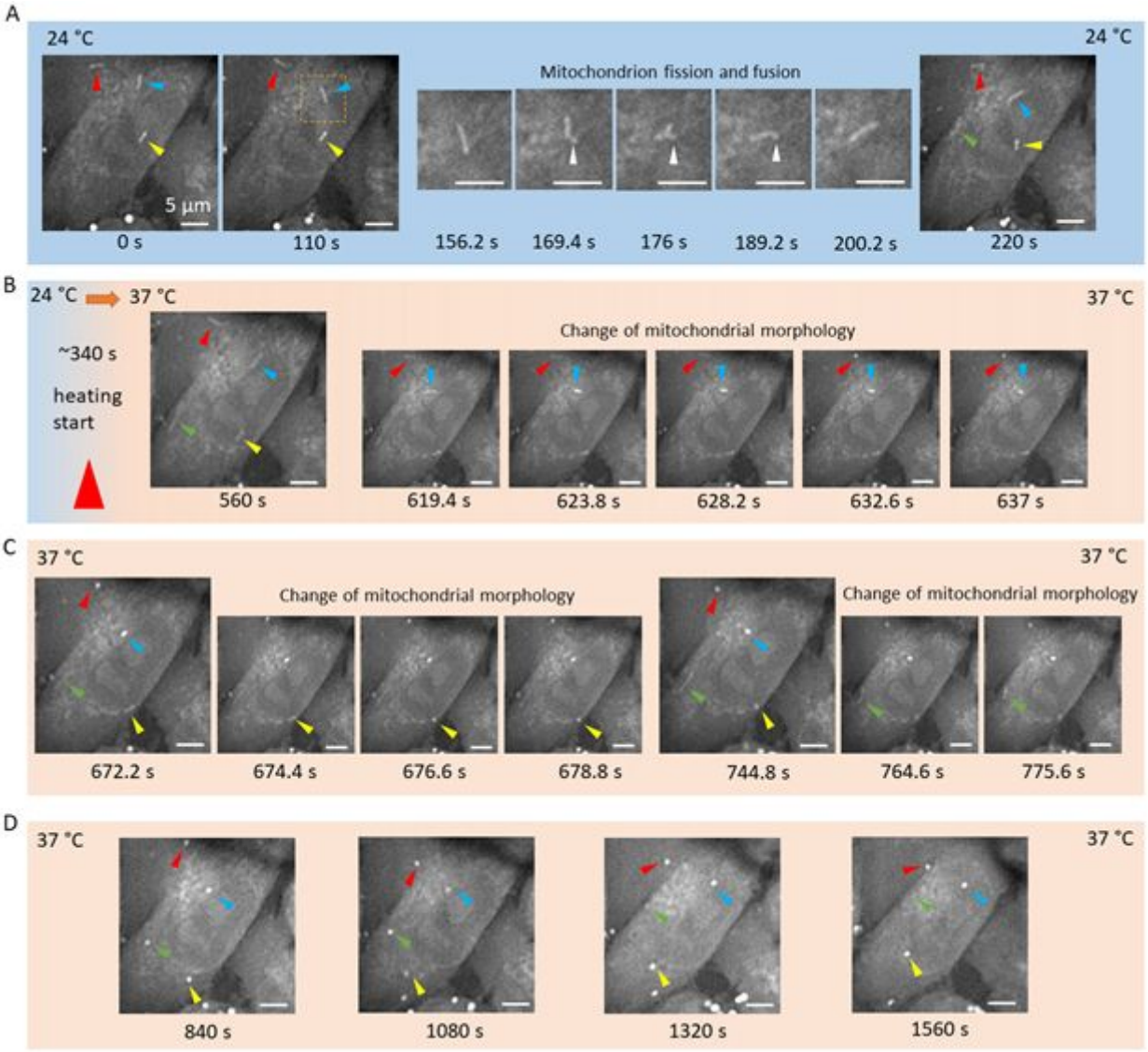

Figure 4

Time-lapse CARS images of a MIAPaCa-2 cell rewarming from hypothermia exposure at 24 °C to physiological temperature at 37 °C. (A) Imaging of the cell began in the hypothermia environment (24 °C). Rod-like FA-accumulated mitochondria were observed (colored arrows). Mitochondria fission and fusion were also observed from 156.2 s to 200.2 s (white arrows). (B) Rewarming started at ~340 s. Two FA-accumulated mitochondria were observed to change their structures. (C) Two additional FA-accumulated mitochondria were observed to change their structures. (D) All four FA-accumulated mitochondria exhibited dot-like morphology. Scale bars represent 5 μm and apply to all images in the sequence.

Supplementary Files

This is a list of supplementary files associated with this preprint. Click to download.

- Supplementaryinformation.docx

- VideoS1A.avi
- VideoS1B.avi
- VideoS2.avi
- VideoS30220s.avi
- VideoS310801300s.avi
- VideoS313201540s.avi
- VideoS315601780s.avi
- VideoS3560780s.avi
- VideoS38401060s.avi